KRITTIKA SUMMER PROJECTS 2025

Analysis of Thermonuclear Bursts in LMXB, 4U 1705-44

Tanishk Mohan, Bhuvanesh K, Vihang Vidwans, Bharat Arora, Rachit Ahuja, Arya Sarode, and Anirudh Salgundi

KRITTIKA SUMMER PROJECTS 2025

Analysis of Thermonuclear Bursts in LMXB, 4U 1705-44

Tanishk Mohan[1], Bhuvanesh K[2], Vihang Vidwans[3], Bharat Arora[4], Rachit Ahuja[5], Arya Sarode[6], and Anirudh Salgundi[1]

[1]Department of Physics, IIT Bombay

[2]Aerospace Department, IIT Bombay

[3]Electrical Engineering, IIT Bombay

[4]Metallurgical Engineering and Materials Science, IIT Bombay

[5]Chemical Engineering, IIT Bombay

PUBLISHED BY KRITTIKA: THE ASTRONOMY CLUB OF IIT BOMBAY
GITHUB.COM/KRITTIKAIITB
First Release, August 2025

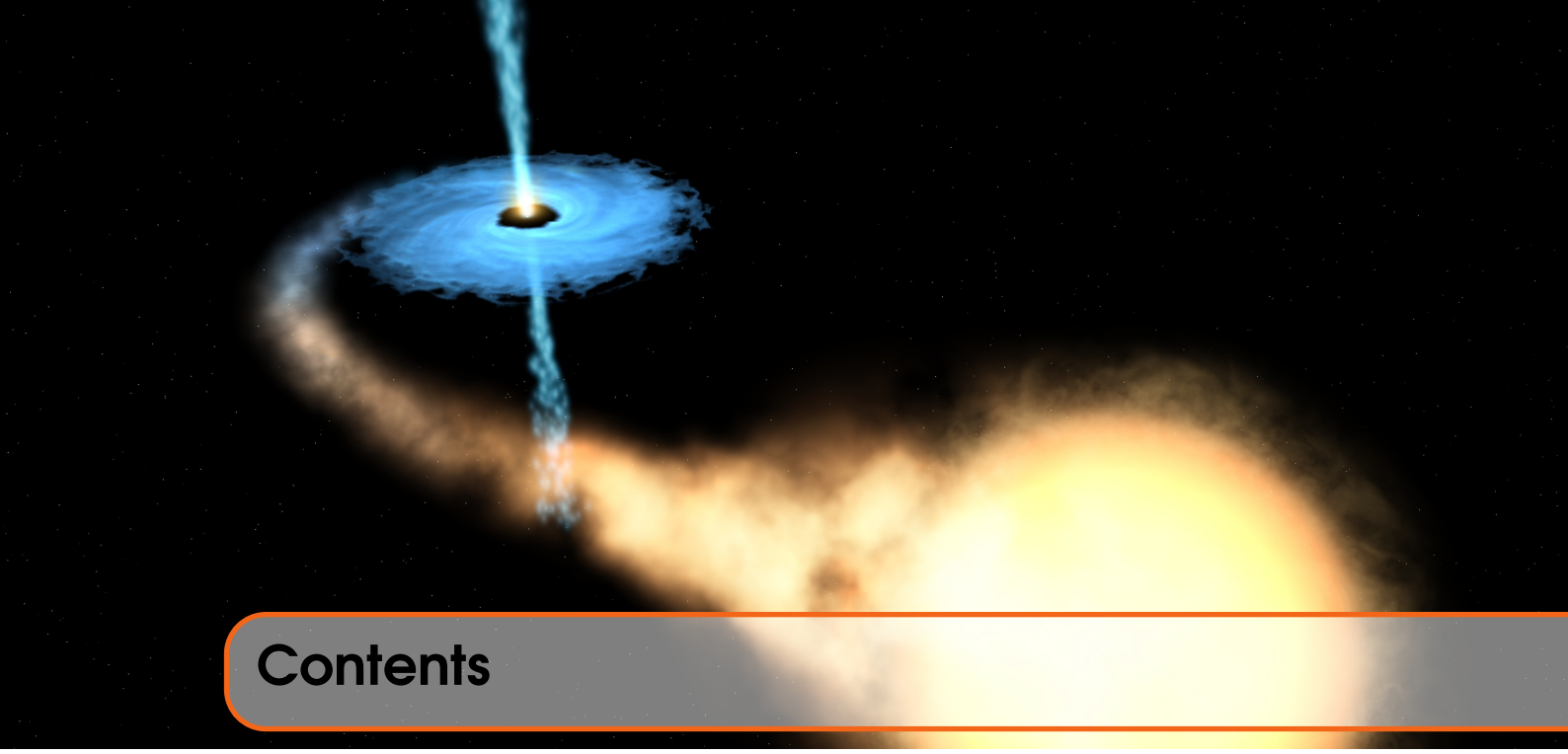

Contents

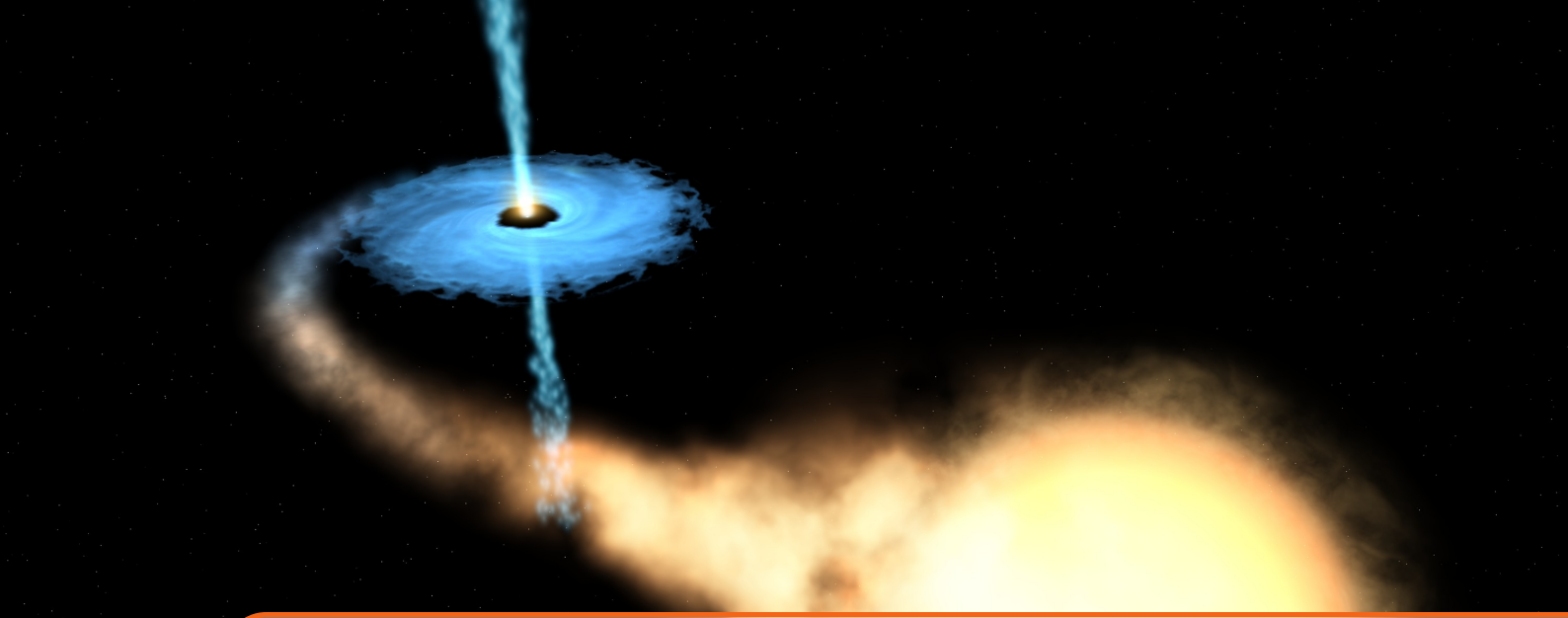

1. Introduction and Theory

1.1 Introduction

1.1.1 Neutron Stars

Neutron stars are the collapsed core of massive supergiant star. Neutron stars have a density of atomic nuclei; Neutron stars are the second smallest and densest stellar object next to black holes. These stars have a radius on the order of 10 km and have a mass around 1.4 solar masses. The stars which collapse into a neutron star have 10-25 solar masses.

1.1.2 Formation

Stars constantly burn there nuclear fuel through fusion processes to produce higher elements starting from hydrogen and helium till iron in their core, once all the nuclear fuel is consumed and formed iron the fusion process cannot undergo anymore because fusing iron requires energy rather giving out energy and due to this the outer layers of the start collapsing towards the core as there is no radiation pressure or electron degeneracy pressure to hold the outer layers by balancing the gravitational force pulling them to the centre. All the matter hits the core and bounces back causing a supernova explosion the brightest events in the universe. This causes the star to die there are different kinds of supernova explosions, supernova 1a disintegrates the whole star leaving nothing behind whereas only supernova 2b explosions leads to the formation of a compact star (These is either a neutron star or a black hole). The formation of the neutron star or a black hole depends on the mass of the dying star if it's less than the Chandrashekar limit it will not form a compact star whereas if it's between 10-25 solar masses form neutron stars and the stars with mass 20-25 solar masses form a black hole.

1.1.3 Internal structure and mechanisms holding the star from collapsing under its own Gravity:

The star is so dense that a spoon of neutron star material has a mass of 3 billion tones. The Neutron star's surface has an enormously high temperature when formed initially around ten million Kelvin but eventually cools down as neutron stars generate no new heat through fusion. These stars sometimes possess very high rotational speed due to conservation of angular momentum.

The Neutron Stars are supported by neutron degeneracy pressure and nuclear forces from the collapse by its own gravity, but there is a limit beyond which these two agencies of pressure are unable to with stand the gravitational force and the neutron star turns into a blackhole this limit is called Tolman–Oppenheimer–Volkoff limit which ranges from 2.2–2.9$M_{\odot}$ if the remnant star has a mass exceeding this limit the star collapses into a blackhole.

1.1.4 Neutron degeneracy pressure:

This comes from the fermi gas model. The fermi gas model is a theoretical model describing a collection of many non-interacting fermions (fermions- particles with half integer spin such as electrons, protons and neutrons that obey Fermi – Dirac statistics)

The requirement for applying the fermi gas model is high density and very low temperature compared to the potential well around it and the presence of sea of free-flowing fermion. Thus, neutron star is an eligible candidate to apply this model as it has very high densities similar to that of an atomic nucleus and the immense gravitational field around the star acts as the potential well and its magnitude is way higher than the temperatures at the core and thus the low temperature assumption is also valid due to very high pressure all the electrons combine with the protons to form additional neutrons thus making it a sea of only free neutrons, applying this model explains most of the structural physics of the neutron star especially how it is able to avoid collapsing into a blackhole.

Key Features of fermi gas model:

- Fermions are subject to Pauli-exclusion principle. This principle fundamentally shapes the properties of the fermi gas
- Idealisation – The fermi gas is an idealised model, assuming no interactions between the particles except those enforced by the exclusion principle

The contribution from the neutron degeneracy pressure is not enough to hold the star stable beyond 0.7 solar masses therefore there is another force which comes into play called the nuclear strong forces which act as repulsive forces when the subatomic particles come closer than 0.8fm, due to the immense pressure inside the core this force also contributes to resist the gravity on the whole with the degeneracy pressure.

1.1.5 Identification of neutron stars:

Isolated neutron stars are usually found by the thermal radiation they emit after their formation as they have very high surface temperatures but as the star cools

overtime the detection of such isolated neutron star becomes difficult. A set of neutron stars sometimes are in a binary star system where one of the star being itself and the other companion star, in such cases the neutron star accretes matter from the companion star and forms a disc around it, due to viscous friction among the particles of the matter the disk starts emitting radiations mainly in the x-ray region and the accreted matter which hits the surface of neutron star when it attains critical temperature and pressure it undergoes a thermal runaway reaction which also emits radiation in a broad spectrum mainly concentrated in the x-ray region these type of neutron binary star systems are called X-ray binary star systems. In the binary star system, the compact star can also be a blackhole along with a companion star.
There are two types of X-ray Binary systems:

- Low mass X-ray Binary star system
- High mass X-ray Binary star system

X-ray Binaries are very important as they serve as the laboratories to in understanding the physical mechanisms behind the accretion and the nature of the compact object with good proximity of observations

1.1.6 X-Ray Binary Systems:

Low-mass X-ray binaries (LMXBs) are binary stellar systems in which a compact object, typically a neutron star, accretes matter from a companion star of comparatively low mass (generally less than about 1–2 solar masses systems with donor masses up to ~10 $M_\odot$ are sometimes included). These systems are the endpoint of binary stellar evolution, involving mass exchange, angular momentum loss, and often a common envelope phase. The key feature distinguishing LMXBs from their high-mass counterparts is the mechanism of mass transfer: while high-mass X-ray binaries (HMXBs) predominantly rely on powerful stellar winds from massive O/B-type companions, LMXBs primarily involve Roche lobe overflow (RLOF) as the dominant channel for matter accretion.
RLOF occurs when the companion star loses it's mass through distortions in the photospheric surface caused due to the compact object being within the Roche-Limit. Once the outer layers of the companion cross this boundary, material begins to flow through the first Lagrangian point (L1) into the gravitational well of the neutron star. This matter cannot fall directly onto the neutron star due to the conservation of angular momentum. Instead, it spirals inward, forming a geometrically thin and almost opaque accretion disk around the compact object. As the gas loses angular momentum through viscous interactions within the disk the gravitational potential energy is converted into thermal energy and emitted primarily in the X-ray band.
Upon reaching the innermost regions of the accretion disk, the material eventually plunges onto the neutron star surface. Here, due to extreme surface gravity, the falling material releases a substantial amount of gravitational energy, on the order of ~100–200 MeV per nucleon. This energy is radiated away as high-energy X-ray photons, often via mechanisms analogous to bremsstrahlung and Compton scattering. The precise radiation spectrum and variability characteristics depend on several factors, including the neutron star's magnetic field, spin frequency, and the geometry of the inner accretion flow. In systems with stronger magnetic fields ($\sim 10^9$ Gauss), accretion columns may form along magnetic poles, while in weaker-field systems ($\sim 10^7$ Gauss), the disk may extend nearly down to the stellar

surface with minimal disruption.
The observed X-ray luminosities of LMXBs typically range between 10^{36} and 10^{38} erg/s, corresponding to accretion rates of roughly 0.01 to 1 times the Eddington accretion rate. This luminosity is modulated on a variety of timescales due to instabilities in the disk, thermonuclear processes on the neutron star surface, and interactions between the accretion flow and the star's magnetic field. Notable phenomena associated with LMXBs include quasi-periodic oscillations (QPOs), which are thought to arise from instabilities or resonance phenomena in the inner disk; Type-I thermonuclear X-ray bursts, which result from unstable ignition of accreted material on the stellar surface; and aperiodic noise and flickering linked to stochastic fluctuations in the accretion rate. (2)
The inclination angle of the system also plays a role in determining the observed spectral features, including dips, eclipses, and reprocessing signatures in soft X-rays or UV.
Because of the high absorption of soft X-rays by the Earth's atmosphere, observations of LMXBs must be conducted using space-based observatories such as RXTE, Chandra, XMM-Newton, and AstroSat.

1.1.7 Accretion Physics

Power Of Accretion

Among the two sources of radiation emission (Nuclear Fusion and the accretion disk) from the X-ray Binaries the radiation emitted by the accretion disk is most efficient and powerful mechanism for producing the high energy radiation in X-ray Binaries. For a body of mass M and radius R the gravitational potential energy released by the accretion of mass m on to its surface is given by:

$$\Delta E_{acc} = \frac{GMm}{R} \tag{1.1}$$

Where G is the Gravitational constant. If the neutron star has a radius as 10km and a mass of 1 solar mass then the energy released is about 10^{20} erg per accreted gram which is large compared to the energy release due to the nuclear fusion of hydrogen into helium in the runaway reaction

$$\Delta E_{nuc} = 0.007mc^2 \tag{1.2}$$

The luminosity resulting from the accretion depends on the rate at which the gravitational energy is released. It is given by

$$L = \frac{GM\frac{dM}{dt}}{R} \tag{1.3}$$

Eddington Limit:

The electromagnetic radiation produced exerts pressure on the material which is proportional to the f lux F of the radiation. If the luminosity is large enough for the radiation to overcome the gravitational potential of the compact object, then the accretion is stopped. This luminosity at which the accretion of matter is stopped is called the Eddington Luminosity and is given as

$$L_E = \frac{4\pi GMm_p c}{\sigma_0}$$

Where σ_0 is the Thomson scattering cross-section, M is the mass of the compact star, mp is the mass of the proton, c is the velocity of light. Substituting the values of the constants in the above equation we get

$$L_E = 1.3 \times 10^{38} \left(\frac{M}{M_\odot} \right) \text{erg/s}$$

Theory of accretion disk:
A relation between the rate of accretion and the radius of the accreted matter is derived by assuming a thin and steady accretion disk in Newtonian gravity. As the accretion disk is thin, we take cylindrical coordinates and use the conservation laws that are the Navier-Stokes equation and the continuity equation. Solving these two equations gives us the relation between rate of accreted mass and radius of the accreted matter around the star.

$$\frac{\partial \Sigma}{\partial x} + \frac{1}{r} \frac{\partial (r \Sigma v_r)}{\partial x} = 0 \tag{1.4}$$

$$\frac{\partial (\Sigma r^2 \Omega)}{\partial x} + \frac{1}{r} \frac{\partial (r^3 \Omega v_r)}{\partial x} = \Lambda \tag{1.5}$$

Let Σ denote the surface density of the accretion disk, $\Omega = \frac{v_\theta}{r}$ the angular velocity, and Λ a term involving viscosity and the redistribution of angular momentum.
Solving the conservation equations of mass and angular momentum with appropriate boundary conditions yields:

$$\nu \Sigma = \frac{\dot{m}}{3\pi} \left[1 - \left(\frac{r_{\text{in}}}{r} \right)^{1/2} \right] \tag{1.6}$$

Here, ν is the kinematic viscosity, $\dot{m}$ is the mass accretion rate, r is the radial distance from the compact object, and r_{in} is the inner edge of the accretion disk.

This expression implies that viscous dissipation in the disk leads to the release of gravitational potential energy, which is ultimately radiated as thermal emission. Since the disk is expected to be optically thick and geometrically thin, it is assumed to emit approximately as a blackbody.

Thus, the effective surface temperature of the disk as a function of radius is given by:

$$T(r) = \left\{ \frac{3GM\dot{m}}{8\pi r^3 \sigma} \left[1 - \left(\frac{r_{\text{in}}}{r} \right)^{1/2} \right] \right\}^{1/4} \tag{1.7}$$

Here, G is the gravitational constant, M is the mass of the compact object (typically a neutron star), and σ is the Stefan-Boltzmann constant.

1.2 X Ray Variabilities in Low Mass X Ray Binaries

Outbursts

Outbursts in low-mass X-ray binaries (LMXBs) are large-scale increases in luminosity, originating from changes in the accretion disk structure. These episodes typically

last from days to several months and are characterized by sudden surges in accretion rate. LMXBs alternate between two distinct states: a quiescent state, in which the source remains faint and stable for extended periods (months to years), and an outburst state during which the luminosity increases dramatically. The prevailing explanation attributes this transient behavior to the disk instability model (DIM), wherein the accretion disk undergoes thermal and viscous instabilities that lead to cyclic transitions between low and high mass accretion rates.

Quasi-Periodic Oscillations (QPOs)

QPOs are observed as features in the power density spectra of LMXBs and reflect modulations in X-ray intensity on timescales ranging from milliseconds to seconds. One proposed explanation is the beat-frequency model, which attributes the modulation to the interaction between the neutron star's spin and the Keplerian orbital frequency at the inner edge of the accretion disk. Clumps of matter orbiting near the magnetosphere modulate the X-ray emission as they accrete.

Thermonuclear X-ray Bursts

Thermonuclear (Type-I) X-ray bursts are sudden increases in X-ray luminosity caused by the unstable ignition of accreted material on the neutron star surface. The fuel originates from the companion star and is transferred via Roche lobe overflow through an accretion disk. Upon reaching the neutron star surface, the matter spreads laterally and accumulates under extreme gravity. Compression raises pressure and temperature until the conditions for nuclear fusion are satisfied, leading to a runaway thermonuclear reaction.

Runaway Thermonuclear Reaction and Ignition Conditions

The depth at which ignition occurs is characterized by the depth of the column $y(r)$, defined as:

$$y(r) = \int_r^\infty \rho(r')\, dr'$$

where ρ is the local mass density. The pressure in the thin outer envelope is given by $P = gy$, under the assumption of hydrostatic equilibrium and constant gravitational acceleration g. Once a critical depth is reached, temperature-sensitive fusion reactions are triggered, primarily via the triple-alpha process for helium or the CNO cycle for hydrogen.

The thin-shell instability prevents the outer layers from expanding and cooling effectively. As the temperature increases, the nuclear reaction rates increase rapidly, driving further heating and sustaining the runaway. This leads to a burst of X-ray emission with a fast rise time (0.5 to 2 seconds) and an exponential decay phase lasting 10 to 100 seconds.

Stability of Nuclear Burning

The transition between stable and unstable nuclear burning is governed by the relative temperature sensitivities of heating and cooling. Thermonuclear instability occurs when:

$$\frac{d\varepsilon_{\text{nuc}}}{dT} > \frac{d\varepsilon_{\text{cool}}}{dT}$$

where ε_{nuc} and $\varepsilon_{\text{cool}}$ represent the specific nuclear heating and radiative cooling rates, respectively. Hydrogen burning via the hot CNO cycle becomes stable at temperatures exceeding $\sim 0.7 \times 10^8$ K due to β-decay rate limitations, whereas helium burning via the triple-alpha process stabilizes at $\sim 3 \times 10^8$ K. The precise ignition regime depends critically on the local accretion rate, as compression heating scales with $\dot{M}$, influencing whether the fuel accumulates slowly for bursts or burns steadily in persistent emission.

1.3 Instrument Details

1.3.1 AstroSat and High-Energy Astrophysics

AstroSat, India's dedicated astronomy satellite, was launched by ISRO on September 28, 2015. It hosts a suite of instruments that span from the ultraviolet to hard X-ray regimes, enabling simultaneous multi-band observations of cosmic phenomena. Among these, the *Large Area X-ray Proportional Counter (LAXPC)* plays a very important role in high-energy astrophysics, particularly in the study of compact objects.

1.3.2 LAXPC: Large Area X-ray Proportional Counter

The LAXPC instrument consists of three co-aligned proportional counter units: LAXPC10, LAXPC20, and LAXPC30. Each unit is composed of multiple layers of anode cells that are sensitive to X-rays in the energy range of 3 to 80 keV. The detectors are built with a multi-layer structure for capturing photons across a wide energy band. Together, the three units provide a total effective area greater than 6000 cm^2.

The energy resolution of the system is approximately 12% at 22 keV, which allows for basic spectral discrimination across the energy band. However, the principal strength of LAXPC lies in its time-axis resolution, which is around 10 μs. This level of precision permits the detection and detailed study of rapid variability in X-ray sources, including millisecond oscillations, Type-I thermonuclear bursts.

Each detector is capable of individual pulse height analysis. This allows for the construction of light curves in selectable energy bands, which can be tuned by the observer depending on the specific scientific objective. The design also includes a field of view of approximately one $degree^2$, which enables effective monitoring of bright X-ray sources over long observational periods. Onboard calibration sources are included to track gain variations during flight, ensuring the stability and reliability of long-term data collection.

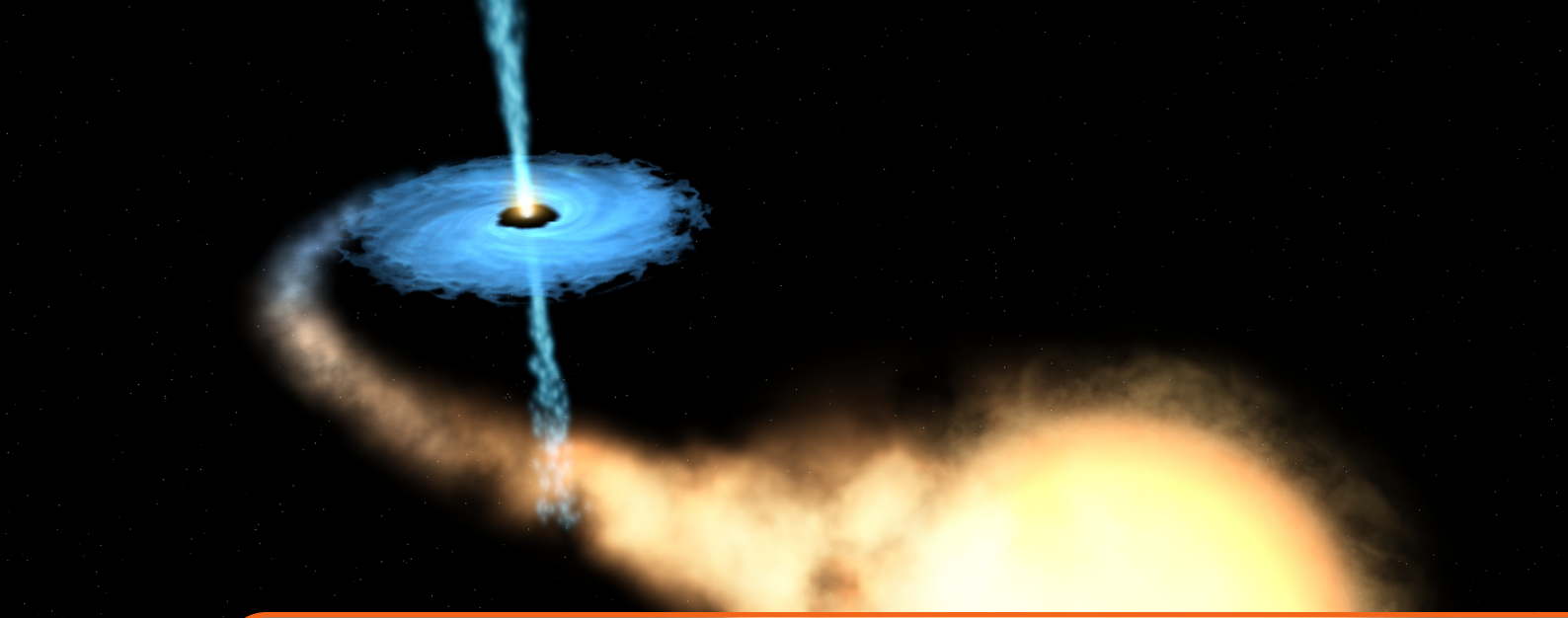

2. Observation and Data Analysis

2.1 Data Acquisition

LAXPC records data using several observational modes, with the most significant being the Event Analysis (EA) mode and the Binned Mode (BB). The Event Analysis mode is particularly suitable for time-series studies because it logs every detected photon individually, along with its arrival time, energy channel, and detector-specific information. This enables highly flexible post-processing of the data to extract light curves and spectra across arbitrary energy and time intervals.

The raw data is stored in Level-1 FITS files, which are the standard file format used in high-energy astrophysics. These files typically come in multiple extensions, including event lists and good time intervals (GTIs). The event list includes information for each photon event, such as the exact time of arrival, the anode layer in which it was detected, the pulse height (which corresponds to energy), and the detector unit. The GTI file marks valid periods of observation, excluding intervals affected by satellite passages through the South Atlantic Anomaly, Earth occultation, or other instrument dead times.

In addition, housekeeping files contain data regarding the instrument status, such as detector voltages, temperatures, and timing synchronization markers. These are crucial for calibration and for understanding time-dependent variations in detector performance.

Long-term light curves are fundamental tools in observational high-energy astrophysics, offering a continuous temporal view of the brightness evolution of compact object systems over extended periods. In this study, the long-term X-ray

light curve has been obtained from the Monitor of All-sky X-ray Image (MAXI), a Japanese instrument aboard the International Space Station. MAXI surveys almost the entire sky every 92 minutes in the 2 to 20 keV energy range, making it particularly well-suited for monitoring variable X-ray sources such as neutron star binaries. Its continuous coverage and systematic cadence allow for the detection of both slow modulations and abrupt transitions in flux that are signatures of changes in accretion dynamics or intrinsic source properties.

In low-mass X-ray binaries (LMXBs), long-term light curves are essential for distinguishing between the quiescent and outbursting phases that characterize transient sources. During quiescence, the accretion rate is low and the X-ray flux often falls below detection thresholds, while outburst phases, lasting from weeks to months, involve elevated accretion rates that significantly boost the X-ray luminosity. These phases are interpreted as resulting from thermal-viscous instabilities in the accretion disk, possibly triggered by changes in disk ionization states. By analyzing the MAXI light curve over months or even years, one can constrain burst recurrence intervals, track gradual flux evolution, and identify the onset of new accretion episodes.

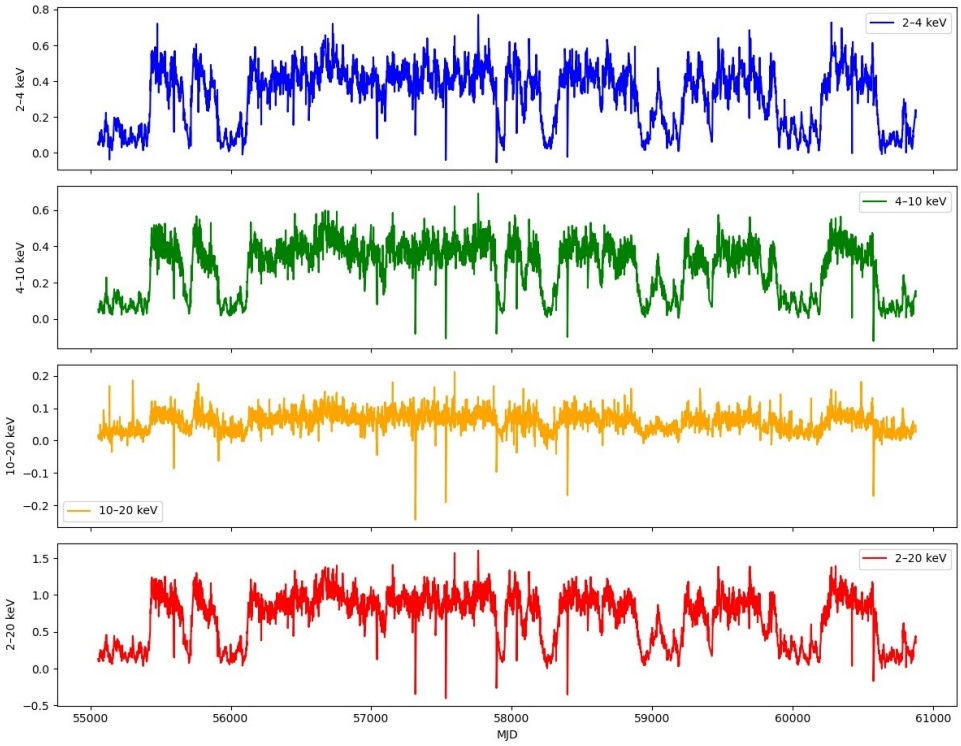

Figure 2.1: Long Term Light Curve in Various Bands from MAXI

Beyond flux monitoring, long-term light curves play a strategic role in observational planning. They allow researchers to select epochs of enhanced activity to conduct high-resolution timing and spectral observations with more sensitive instruments such as LAXPC aboard AstroSat or the NICER instrument on the ISS. For instance, if the light curve indicates sustained activity, one might expect an increased likelihood of Type-I thermonuclear bursts or the appearance of fast timing features such as quasi-periodic oscillations (QPOs). These associations are

supported by historical data and form the basis of multi-instrument campaigns aimed at capturing rare but astrophysically significant events.

To extract deeper insights beyond flux variability, the light curve is complemented with a hardness-intensity diagram (HID). The HID is constructed by plotting the source intensity against its spectral hardness, typically defined as the ratio of count rates in a hard band to those in a soft band. In this context, the intensity is often derived from the total count rate in a broad energy band, while the hardness ratio is calculated from two narrower sub-bands within the instrument's energy range. The HID serves as a powerful empirical diagnostic of source states, especially in neutron star LMXBs where spectral state transitions are correlated with physical changes in the accretion environment.

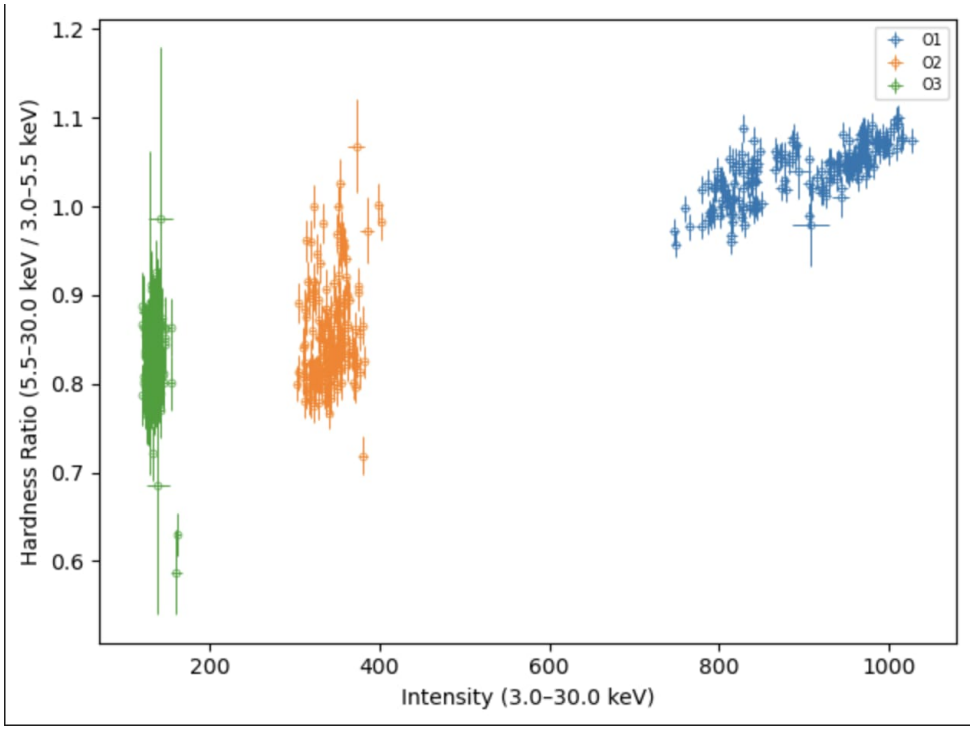

Figure 2.2: Hardness Intensity Curve for each of the three Bursts

In practice, sources follow characteristic tracks in the HID, which correspond to physically distinct regimes. For atoll sources, the transition between the island and banana states reflects variations in the accretion rate and the dominance of Comptonized or thermal emission. Z sources, typically accreting at or above the Eddington limit, display a more complex HID pattern with three branches—horizontal, normal, and flaring—associated with different modes of accretion and changes in inner disk structure. The movement along these tracks often occurs over timescales of hours to days, which can be contextualized by referencing the longer-term behavior seen in MAXI light curves.

The HID is particularly useful for linking spectral changes to timing behavior. In many cases, the onset of a QPO or a change in burst recurrence coincides with a

Obs ID	tstart(mjd)	tstop(mjd)	mean count rate
9000003792 (B1)	59069.084	59069.086	470.130
9000003888 (B2)	59110.629935	59111.238457	773.84
9000003888 (B3)	59110.629935	59111.238457	773.84

Table 2.1: Source Observation ID's with their corresponding, observation start, stop time and mean photon count rates and number of bursts

particular segment of the HID track. For instance, high-frequency QPOs are often associated with intermediate states, while strong broadband noise is prevalent in the hard state. This makes the HID not just a static diagnostic but a dynamic phase-space map that reflects the ongoing evolution of the accretion process.

Moreover, the spectral hardness is relatively insensitive to interstellar absorption, allowing for robust tracking of intrinsic source changes even when absolute flux measurements are uncertain. In sources with complex spectral components, including thermal disk emission, Comptonized coronae, and boundary layer contributions, the hardness ratio can reflect changing dominance among these components. It also enables rapid classification of newly active sources or poorly studied systems by comparison to well-established HID templates.

2.2 9000003792 (B1)

2.2.1 Burst Light Curve Analysis

The neutron star low-mass X-ray binary **4U 1705–44** is a burster known to emit Type-I thermonuclear X-ray bursts due to unstable helium ignition on its surface. During the **AstroSat observation ID - 9000003792**, one such burst was detected, and its light curve was studied to examine its rise, peak, and decay characteristics in detail. The data span the interval from **MJD 59069.084** to **MJD 59069.086**, within which the burst clearly stood out over the persistent count rate.

To study the burst, we processed the level-1 laxpc data using the laxpc pipeline, to obtain level-2 data and then used standard filterfiles to get the **Good Time Intervals** to eliminate background noise, like those from SAA passages and Earth occultation. We then extracted the light curve in the **3–80 keV** range using **1-second bins**. The resulting plot showed a distinct burst with a sharp increase in count rate followed by a slower drop which is a typical feature of a Type-I thermonuclear burst.

A light curve is a starting point for deeper analysis, such as applying the **FRED fit** to extract parameter values of rise and decay times, measuring the **T90 duration** and further analysis. Although detailed rise and decay are not seen in the figure below, the spike marks the burst's presence.

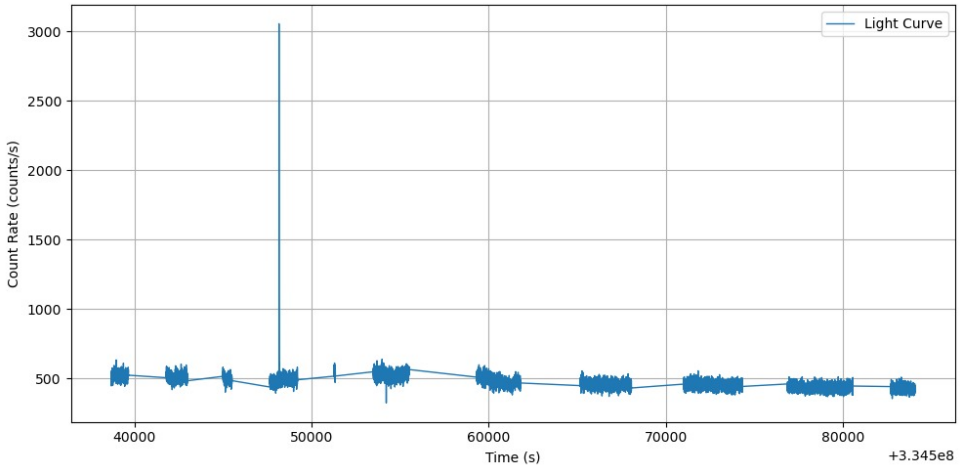

Figure 2.3: Light curve of B1 constructed from the Level-2 FITS file using the Good Time Intervals (GTIs) provided by LAXPC.

2.2.2 Non-Burst and Burst Regions

To study the source's activity, we split the light curve into two separate sections, one without any bursts and another where a clear burst was observed. We applied a technique known as sigma clipping for the non-burst region which helps identify points that significantly deviate from the mean count rate.

The non-burst region shows a fairly constant count rate, which reflects the regular background emission termed persistent emission from the source. The mean count rate of persistent emission is 470.130 counts/s.

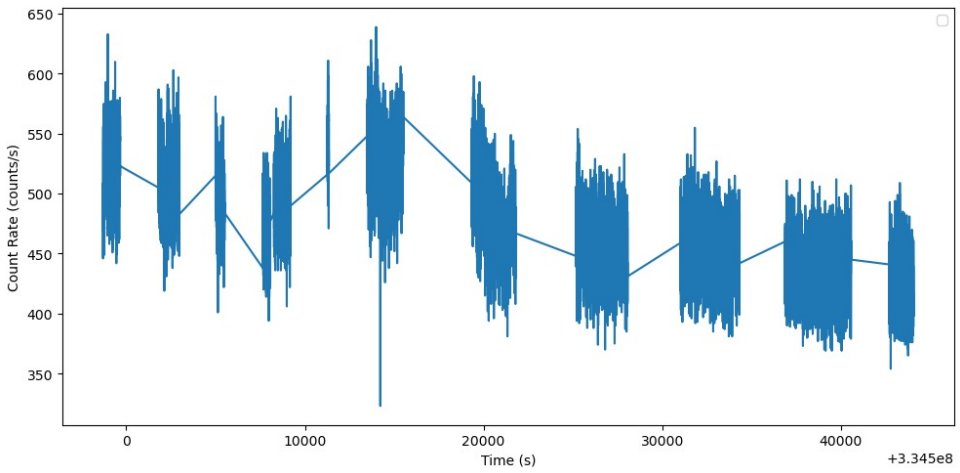

Figure 2.4: Sigma- clipped Non burst light curve segment depicting persistent X-ray emission.

In comparison to this, the burst region shows a sudden and sharp spike count rate followed by slower decay, representing a Type I thermonuclear burst.

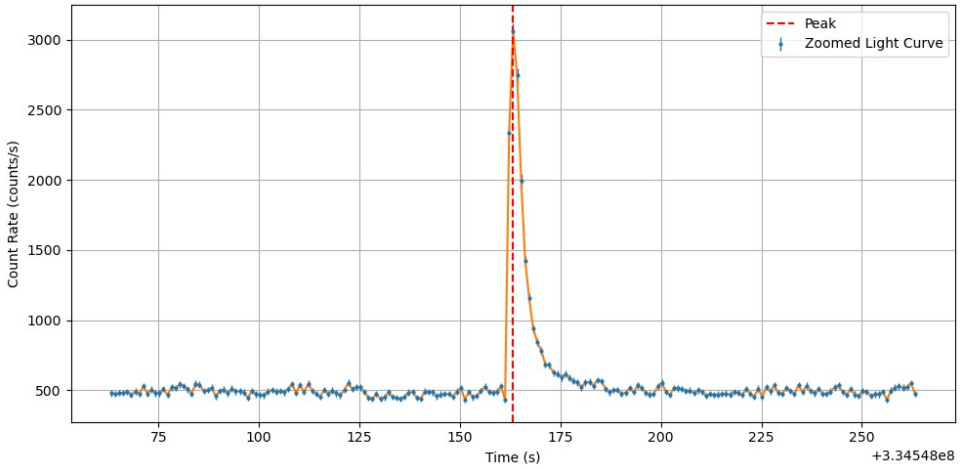

Figure 2.5: Light curve segment from the burst region depicting ± 100 seconds window around the peak count rate representing a Type-I Thermonuclear Burst.

2.2.3 FRED Model Fit

To quantify the burst shape, we applied the Fast Rise Exponential Decay (FRED) model to the burst window light curve segment shown in Fig 2.3:

$$f(t) = \begin{cases} A_{\text{rise}} \cdot \exp\left(\frac{t_{\text{peak}} - t}{\tau_{\text{rise}}}\right) + B, & \text{if } t \leq t_{\text{peak}} \\ A_{\text{decay}} \cdot \exp\left(\frac{t - t_{\text{peak}}}{\tau_{\text{decay}}}\right) + B, & \text{if } t > t_{\text{peak}} \end{cases}$$

2.2.4 Parameters

- $\mathbf{t_{peak}}$: This is the time at which the burst reaches its maximum intensity.
- τ_{rise} : A parameter that characterizes how quickly the signal increases before reaching its peak. A smaller value means a faster rise.
- τ_{decay}:A parameter describing how slowly or quickly the signal decreases after the peak. Larger values indicate a slower decay.
- A_{rise}: The scaling factor or amplitude associated with the rising part of the signal. It affects how steep or high the rising edge is
- A_{decay}: The amplitude associated with the decaying part of the signal. It controls the height or strength of the signal's fall-off.
- **B (Background)**:The constant background level or offset in the signal. It represents the baseline intensity not related to the peak structure.

Parameter	Fitted Value
$\mathbf{t_{peak}}$	334548163 seconds
τ_{rise}	0.669 seconds
τ_{decay}	3.248 seconds
A_{rise}	2698.182 counts/s
A_{decay}	2686.368 counts/s
B (Background)	492.086 counts/s

Table 2.2: Fitted Parameters of the FRED model for (O1)

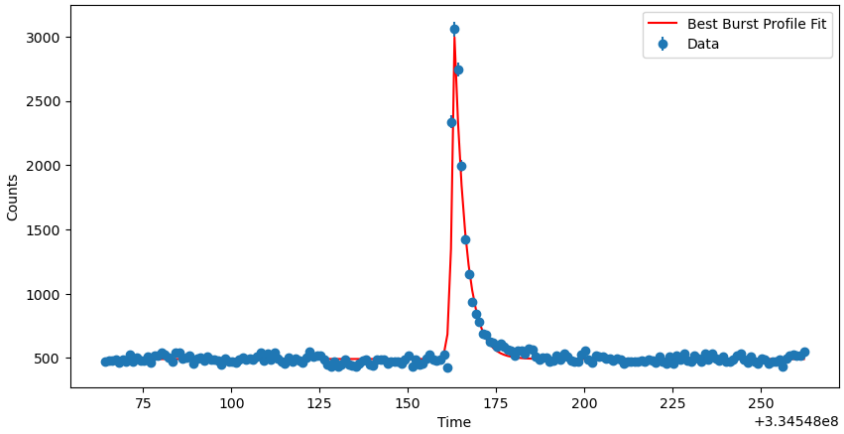

Figure 2.6: FRED model fit to the zoomed-in light curve of B1 with a burst window of ± 100 seconds around the peak count rate.

2.2.5 T90 Duration Estimation

To estimate how long the burst lasted, we calculated the T_{90} parameter. This measures the time during which 90% of the total counts of the burst are observed, specifically, from 5% to 95% of the **cumulative count distribution**

- The **start** of the T90 interval (t_5) is the time at which 5% of the cumulative counts have been recorded.
- The **end** of the T90 interval (t_{95}) is the time at which 95% of the cumulative counts have been recorded.

$$T_{90} = t_{95} - t_5$$

The cumulative count curve and the T_{90} interval are shown in Figure 2.5.
In our case:

$$t_5 = 334548162.232 \text{ s}$$
$$t_{95} = 334548171.232 \text{ s}$$
$$T_{90} = t_{95} - t_5 = 9.000 \text{ s}$$

This gives us a burst duration of **9 seconds**.

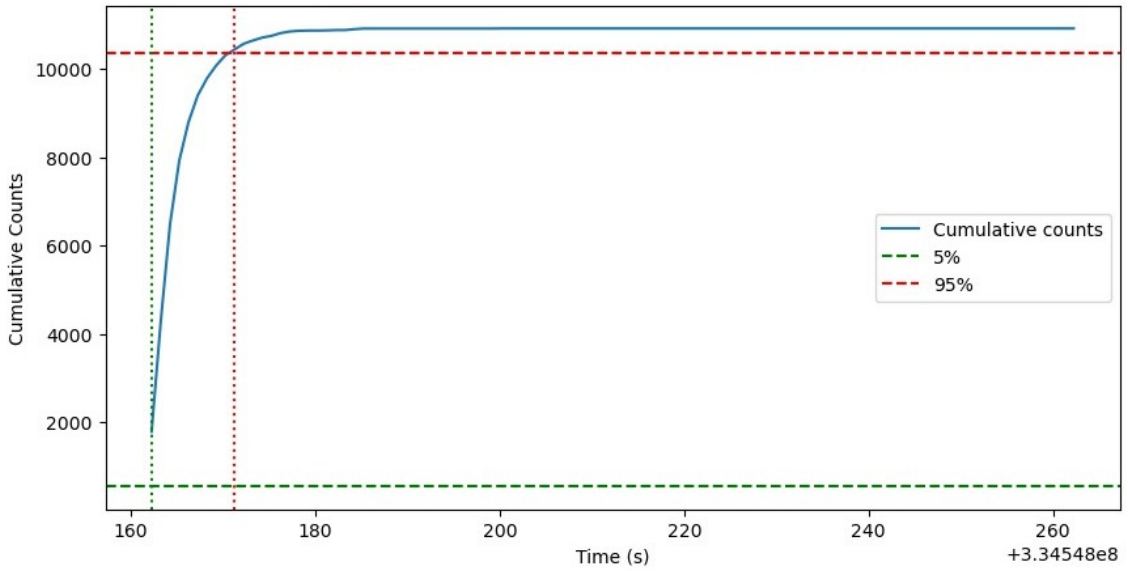

Figure 2.7: Cumulative counts plot for the burst region of B1.

2.3 9000003888 (B2)

2.3.1 Initial Analysis

Light Curve

Burst 2 was observed in event `20200918_A09_044T01_9000003888` of neutron star 4U 1705−44 by AstroSat.
The light curve for this event is shown below:

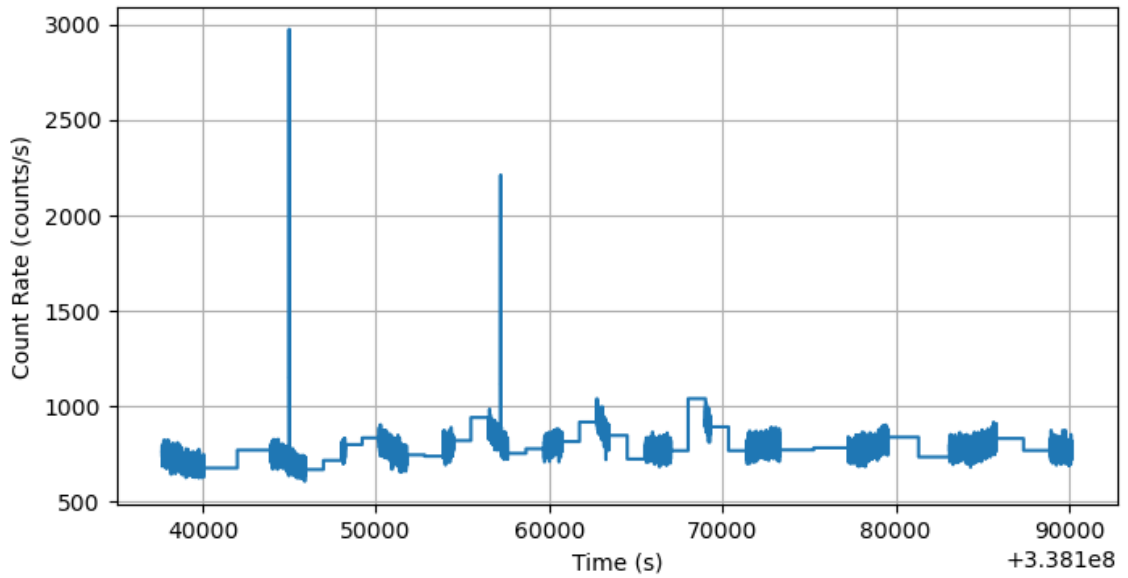

Figure 2.8: Light curve of event `20200918_A09_044T01_9000003888`, constructed from the Level-2 FITS file using the Good Time Intervals (GTIs) provided by LAXPC.

The following graph shows 2 thermonuclear (type-I) bursts. We will be focusing on the first burst of the light curve.

Finding Peaks

The first part of the analysis is to locate bursts in the light curve and identify our target burst.
This can be done using the `find_peaks` function from the `scipy.signal` module in Python. We specify a threshold peak height and a minimum distance between peaks to isolate individual burst events.
The function used is:

```
peaks, properties = find_peaks(rate, height=2000, distance=20)
```

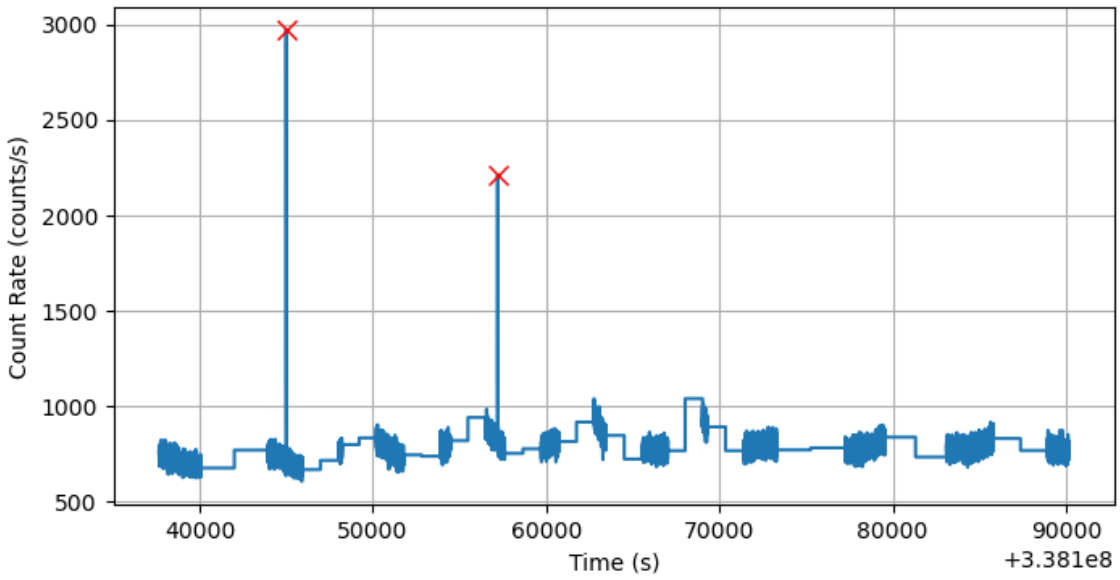

Figure 2.9: Detected peaks in the light curve of event `20200918_A09_044T01_9000003888`, constructed from the Level-2 FITS file using the Good Time Intervals (GTIs) provided by LAXPC.

Results:

The peak detection algorithm identified two candidate bursts:

- **Peak #1:** Time = 338144999.4 s, Rate = 2974.0 counts/s
- **Peak #2:** Time = 338157206.4 s, Rate = 2210.0 counts/s

In this analysis, we focus on **Peak #1**, which corresponds to the primary burst of interest.

2.3.2 Good Time Intervals (GTI)

Burst GTI Plot

To analyze the burst (B2) in detail, we restrict the light curve to a time window centered around the burst peak. Specifically, we consider a Good Time Interval (GTI) ranging from 10 seconds before to 50 seconds after the burst peak time.
This helps isolate the burst from continuous emission.

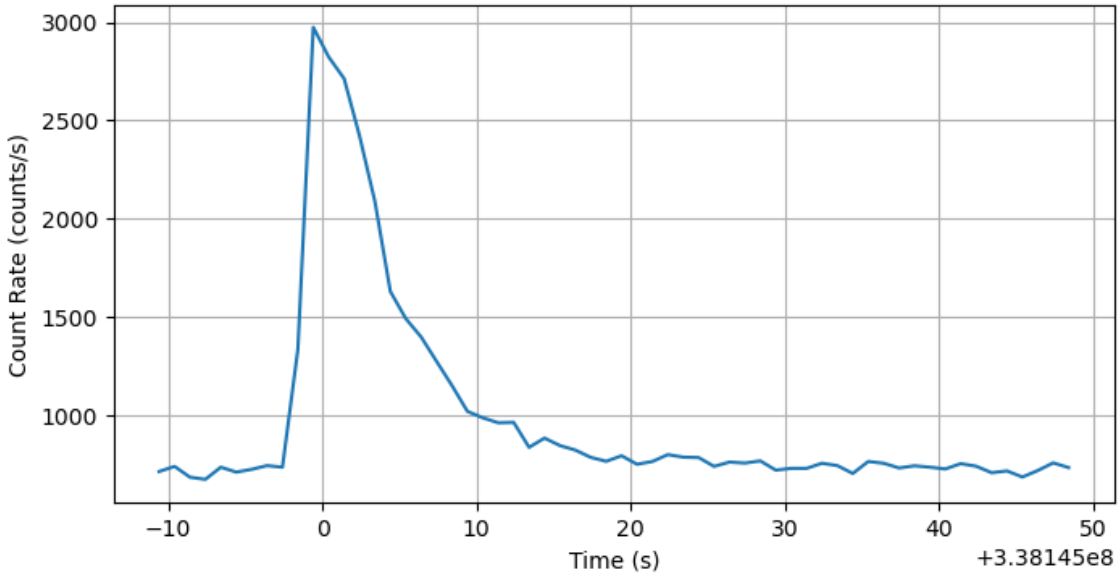

Figure 2.10: Zoomed-in light curve of the B2 in event `20200918_A09_044T01_9000003888`, extracted using a GTI of $[-10\text{s}, +50\text{s}]$ around the burst peak.

GTIs Identification for Non-Burst Regions

To study non-burst emission, we first identify Good Time Intervals (GTIs) that exclude the burst regions. This is done using a two-step process:

1. **Sigma-clipping:** We apply sigma-clipping on the light curve to remove statistical outliers such as bursts. The result is shown below.

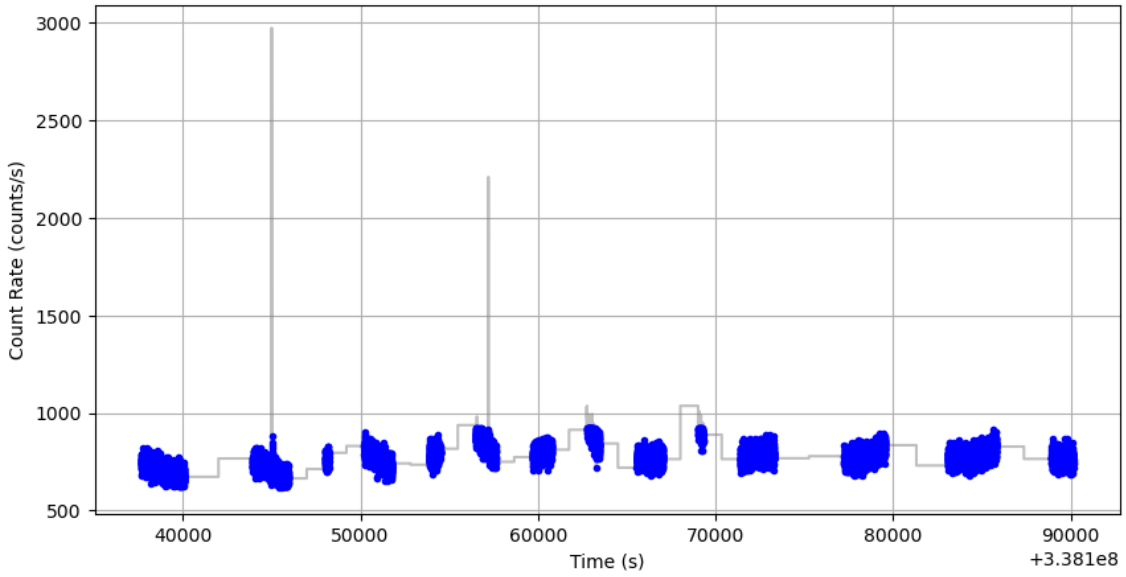

Figure 2.11: Sigma-clipped light curve used to identify background regions by excluding burst outliers.

2. **Segment identification:** We scan through the sigma-clipped curve and identify continuous regions by checking for time gaps between consecutive points. If a gap exceeds a threshold, it is considered a boundary between GTI segments.

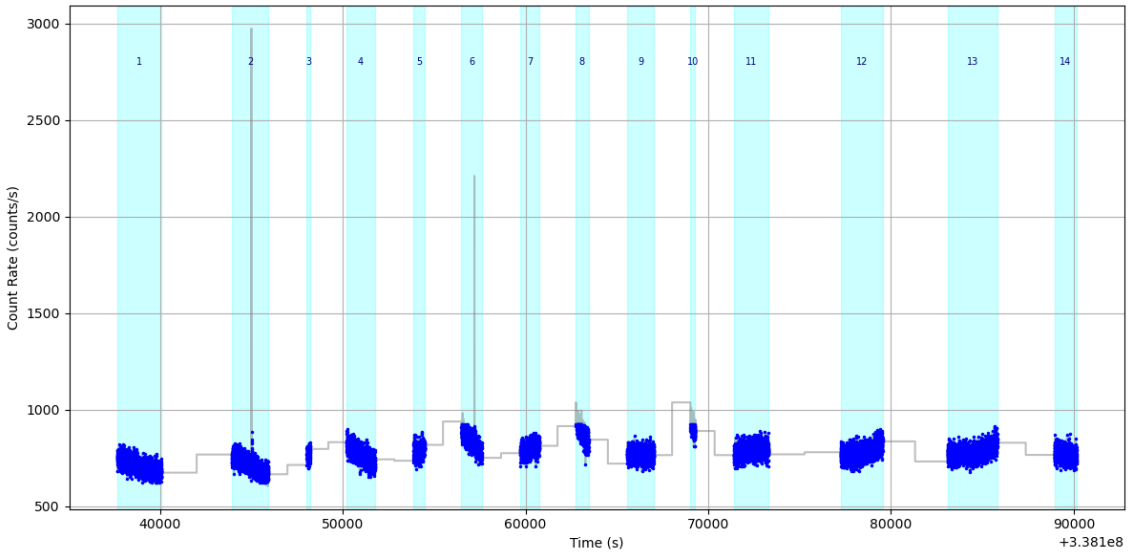

Figure 2.12: Detected non-burst GTI segments overplotted on the sigma-clipped light curve.

The following GTI segments were identified:

- Segment 1: Start = 338137667.4 s, End = 338140074.4 s, Duration = 2407.0 s
- Segment 2: Start = 338143941.4 s, End = 338145919.4 s, Duration = 1978.0 s
- Segment 3: Start = 338148031.4 s, End = 338148211.4 s, Duration = 180.0 s
- Segment 4: Start = 338150216.4 s, End = 338151763.4 s, Duration = 1547.0 s
- Segment 5: Start = 338153876.4 s, End = 338154480.4 s, Duration = 604.0 s
- Segment 6: Start = 338156495.4 s, End = 338157606.4 s, Duration = 1111.0 s
- Segment 7: Start = 338159720.4 s, End = 338160751.4 s, Duration = 1031.0 s
- Segment 8: Start = 338162751.4 s, End = 338163450.4 s, Duration = 699.0 s
- Segment 9: Start = 338165564.4 s, End = 338167022.4 s, Duration = 1458.0 s
- Segment 10: Start = 338169024.4 s, End = 338169294.4 s, Duration = 270.0 s
- Segment 11: Start = 338171408.4 s, End = 338173293.4 s, Duration = 1885.0 s
- Segment 12: Start = 338177253.4 s, End = 338179538.4 s, Duration = 2285.0 s
- Segment 13: Start = 338183097.4 s, End = 338185808.4 s, Duration = 2711.0 s
- Segment 14: Start = 338188942.4 s, End = 338190151.4 s, Duration = 1209.0 s

Next, we exclude the burst intervals by removing a window of ± 50 seconds around the peak time of each identified burst and we subtract an offset of 3.381×10^8 seconds from all time stamps.
The final cleaned GTIs—excluding all burst intervals—are shown below:

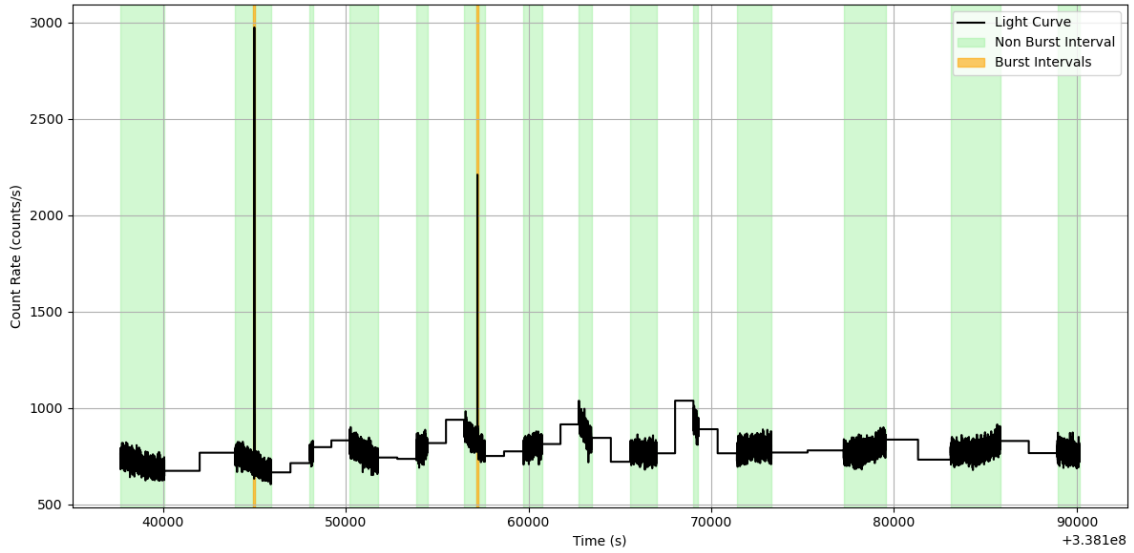

Figure 2.13: Burst and non-burst GTIs: the non-burst GTIs (segments shown in blue) were selected by removing all ± 50 s intervals around burst peaks.

Final GTIs (Good Time Intervals) after burst exclusion:

Start Time (s)	Stop Time (s)	Duration (s)
37667.4	40074.4	2407.0
43941.4	44949.4	1008.0
45049.4	45919.4	870.0
48031.4	48211.4	180.0
50216.4	51763.4	1547.0
53876.4	54480.4	604.0
56495.4	57156.4	661.0
57256.4	57606.4	350.0
59720.4	60751.4	1031.0
62751.4	63450.4	699.0
65564.4	67022.4	1458.0
69024.4	69294.4	270.0
71408.4	73293.4	1885.0
77253.4	79538.4	2285.0
83097.4	85808.4	2711.0
88942.4	90151.4	1209.0

Table 2.3: Final non-burst Good Time Intervals (GTIs) selected after excluding ± 50 s around all burst peaks.

2.3.3 Fast Rise Exponential Decay Model Fit

The Fast Rise Exponential Decay (FRED) model is commonly used to fit gamma-ray or X-ray burst light curves. It captures the characteristic morphology of many bursts, consisting of a rapid rise to peak intensity followed by a gradual exponential

decay.
The FRED function used in this analysis is given by:

$$I(t) = A \cdot \lambda \cdot \exp\left(-\frac{\tau_1}{t-t_s} - \frac{t-t_s}{\tau_2}\right) + C, \quad t > t_s \tag{2.1}$$

where:

- A is the pulse amplitude,
- t_s is the pulse start time,
- τ_1 is the rise timescale,
- τ_2 is the decay timescale,
- C is a offset level from origin line, and
- $\lambda = \exp\left(2\sqrt{\frac{\tau_1}{\tau_2}}\right)$ is a normalization factor.

We fit this function to the light curve using the `scipy.optimize.curve_fit` function in Python which optimize parameters to minimize the residual between the observed count rate and the model.

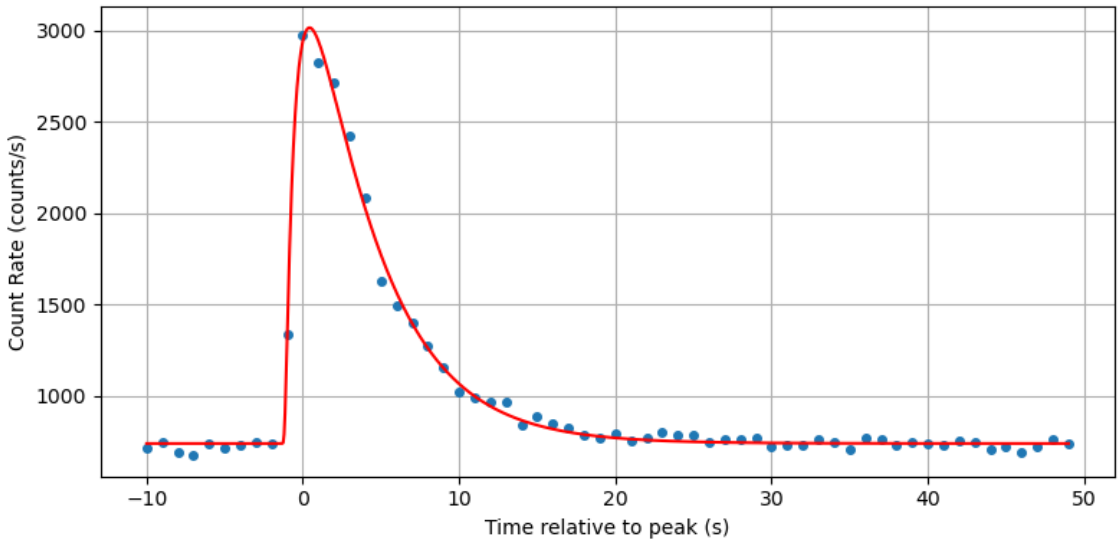

Figure 2.14: FRED model fit to the zoomed-in light curve of the B2 in event `20200918_A09_044T01_9000003888`, extracted using a GTI of $[-10\,\mathrm{s}, +50\,\mathrm{s}]$ around the burst peak.

The optimized parameters obtained from the FRED model fit are listed below:

Parameter	Value
A	2277.69 counts/s
t_s	338099998.63 s
τ_1	0.777 s
τ_2	4.150 s
C	737.19 counts/s
λ	$\exp\left(2\sqrt{\tau_1/\tau_2}\right) \approx 2.376$

Table 2.4: Best-fit parameters for the FRED model

2.3.4 Calculation of T90

The **T90** duration is a standard measure of the temporal extent of a burst. It is defined as the time interval during which 90% of the total burst counts are detected.
Specifically:

- The **start** of the T90 interval (t_5) is the time at which 5% of the cumulative counts have been recorded.
- The **end** of the T90 interval (t_{95}) is the time at which 95% of the cumulative counts have been recorded.

$$T_{90} = t_{95} - t_5$$

This metric helps quantify the burst duration while minimizing the influence of background noise or extended emission tails. It is widely used in gamma-ray and X-ray burst analyses.
The following graph shows the pulse of the FRED model with vertical lines marking t_5 and t_{95}, from which T_{90} is determined:

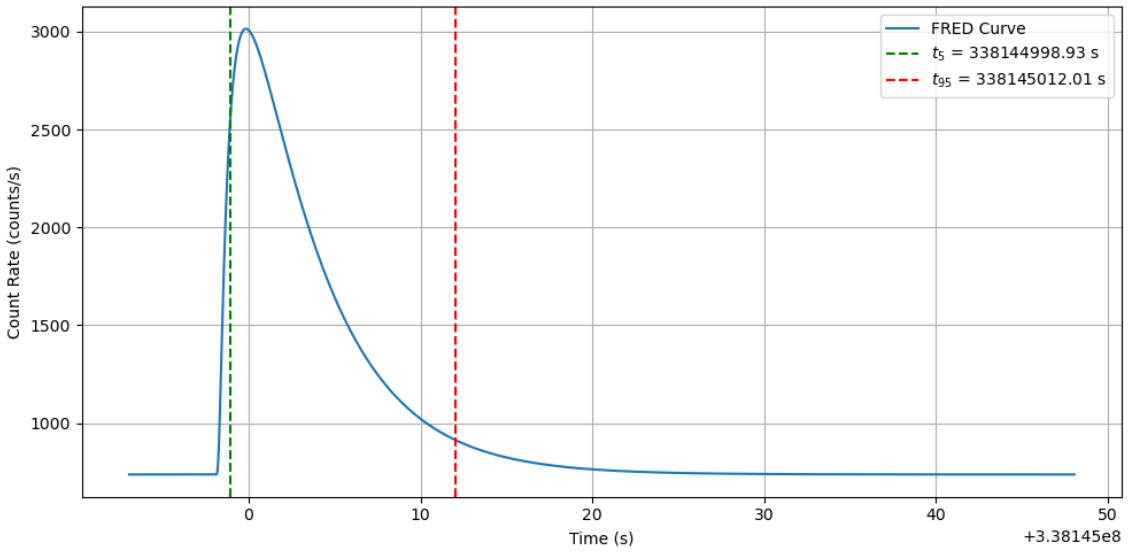

Figure 2.15: FRED model fit with vertical lines at $t_5 = 338144998.93\,\mathrm{s}$ and $t_{95} = 338145012.01\,\mathrm{s}$ used to calculate T_{90}.

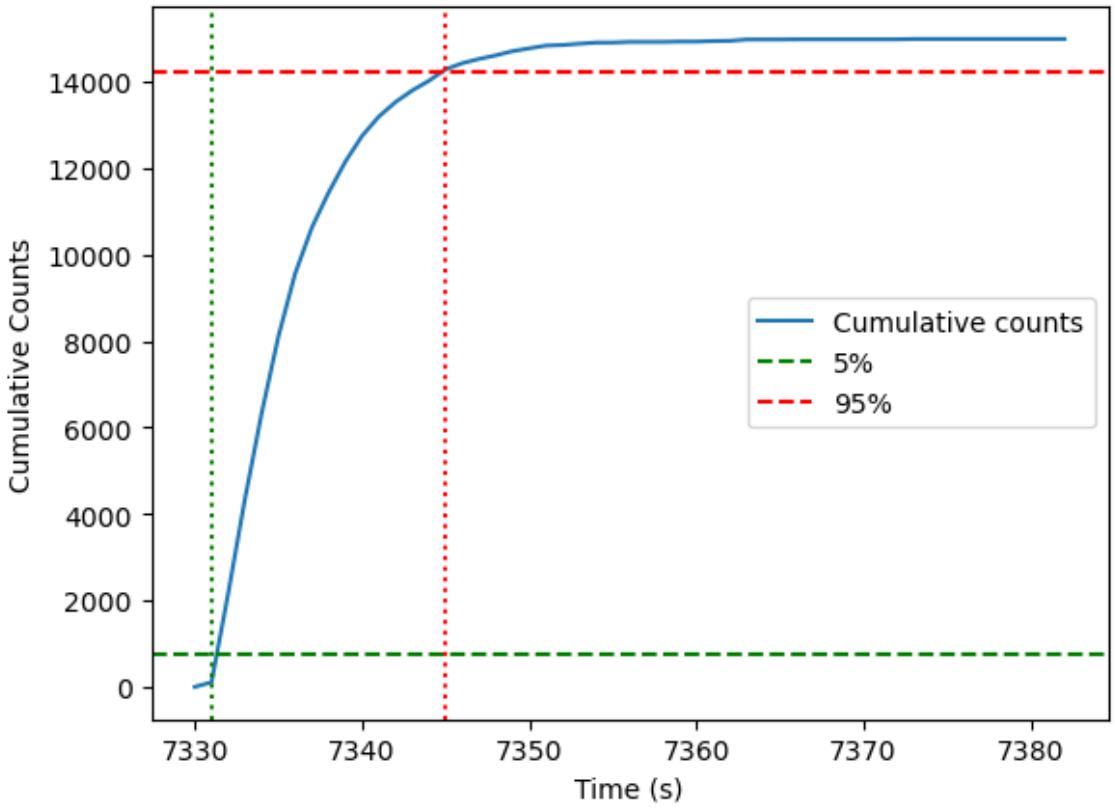

Figure 2.16: Cumulative counts for the burst region (Time is rescaled by subtracting observation start time)

Result:

$$t_5 = 338144998.93 \text{ s}$$
$$t_{95} = 338145012.01 \text{ s}$$
$$T_{90} = t_{95} - t_5 = 13.08 \text{ s}$$

2.3.5 Spectrum and Evolution of Burst Parameters

The T90 obtained in the last section is then further divided into time bins of 1 second each. Every bin is named as a region inside this burst for further analysis.

A function makes the .txt GTI files for each region of the burst. In our case, we are taking 15 such regions out of which 14 are used for the analysis. Primarily we want to generate the spectrum for every region. It will give us the channel number vs counts per second for the photons incident on the detector in the duration of 1 1-second time bin specified by the GTI files.

Spectrum is generated by LAXPC command "laxpc_make_spectra" and it gives a .pha file as the output. The most reliable pcu on the LAXPC is pcu number 2, so we will consider the spectrum generated by this only. One more thing that was done before generating the spectra was to run "laxpc_make_lightcurve" on the region's GTI files. These commands, along with generating lightcurve, changes .txt GTI files

to .fits format, which is a required input format for the command that generated the spectra.

In order to take care of background spectra, a separate GTI file is used for the non-burst region and spectra is generated using the above command.

All of the further analysis is done through HEASOFT's XSPEC terminal. Spectra is fitted by a multiplicative model; tbabs and bbodyrad.
tbabs is the Tuebingen-Boulder ISM absorption model. This model calculates the cross-section for X-ray absorption by the ISM, and nH (equivalent hydrogen column, in units of 10^{22} atoms cm^{-2}) parameter is fixed at 1.42 +- 0.3.
bbodyrad is a blackbody spectrum with normalization proportional to the surface area. It has two parameters, kT (temperature keV) and K(norm), which are kept free.

This multiplicative model is then fit to the spectrum, and these parameters are obtained. A standard template.tcl file is made, which contains a series of common commands applied to the regions of the burst, after the data is loaded for any region of the burst.

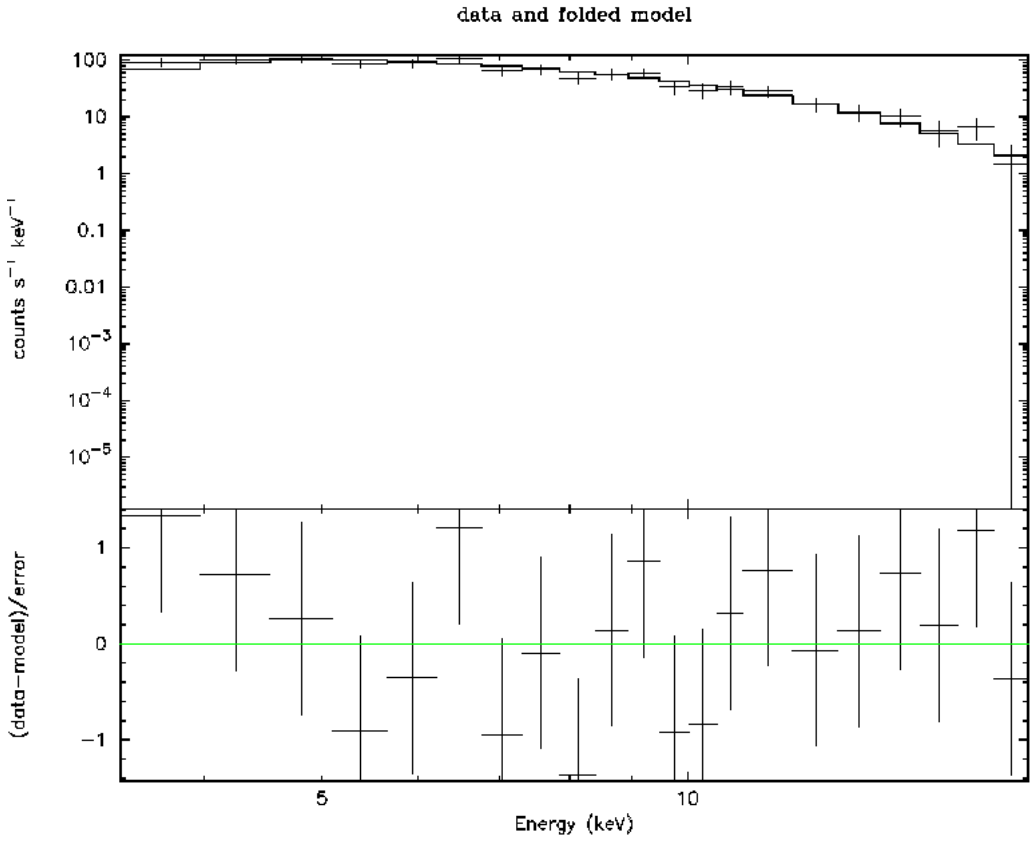

Figure 2.17: tbabs*bbodyrad fit for spectrum of region 2 in the B2

Region	**Temp (keV)**	**Radius (km)**	**Flux ($10^{-9} ergs/cm^2/s$)**	$\Delta\chi^2$
2	2.00047	4.2754	4.7485	$4.4894e{-}02$
3	2.15383	7.1281	18.098	$1.9263e{-}05$
4	2.19842	6.5474	16.659	$4.0526e{-}04$
5	2.05444	7.3381	15.679	$4.6789e{-}03$
6	1.83534	8.2292	12.122	$5.7894e{-}09$
7	1.58795	9.9079	9.2801	$7.4736e{-}05$
8	1.34615	11.8928	6.2967	$3.0263e{-}03$
9	1.29436	11.9293	5.2729	$1.1157e{-}02$
10	1.05485	17.7407	4.3116	$3.1105e{-}02$
11	1.15790	13.0836	3.7211	$5.0500e{-}02$
12	0.946619	19.0509	2.8475	$9.7058e{-}03$
13	0.934931	16.9084	2.1007	$4.6812e{-}02$
14	0.810408	23.4212	1.8442	$3.1947e{-}02$
15	0.811633	21.0603	1.5040	$4.3684e{-}02$

Table 2.5: Temperature, Radius and $\Delta\chi^2$ obtained after fitting the tbabs*bbodyrad model to the spectrum. Energy range 3.0 keV to 20.0 keV is takeFlux is calculated separately in the energy range 3.0 keV to 80.0 keV

After fitting the spectrum with tbabs*bbodyrad model, temperature and norm are obtained for each region. We can calculate the radius from this norm by using the formula given below:

$$\text{norm} = K = \frac{R_{km}^2}{D_{10}^2}$$

where R_km is the source radius in km and D_10 is the distance to the source in units of 10 kpc. D_10 is taken to be 0.76 in the units of 10 kpc.

Flux is calculated by the xspec command given below:

```
1          flux 3.0 80.0 err
```

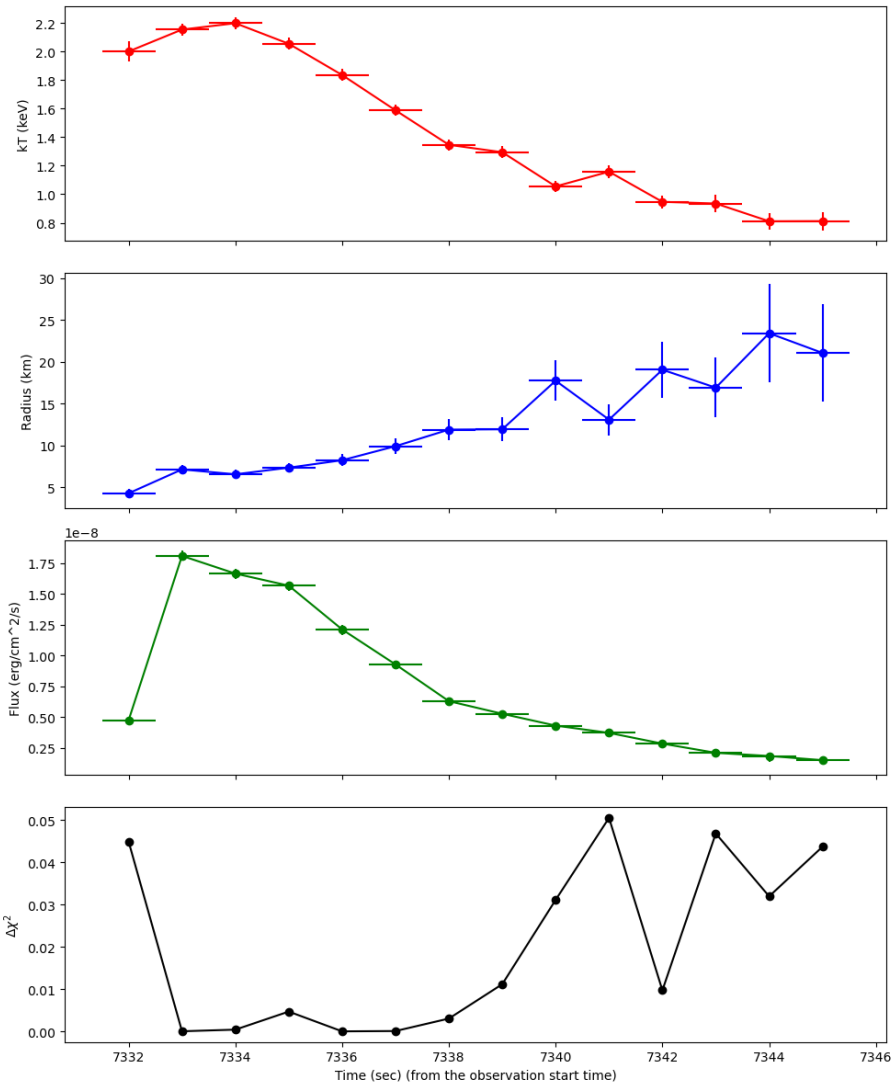

Figure 2.18: Evolution of parameters of the burst with respect to time. Top to bottom; temperature, radius, flux, and $\Delta\chi^2$

By analyzing the time-resolved spectral analysis results of this burst, we tried to find that if this shows the sign of photospheric radius expansion (PRE). By going through the methods given in Galloway et al., we find that this can be a possible candidate for the PRE burst. The anti-correlation between temperature and radius suggests that this might be a PRE type burst.

Kuulkers et al. (2003) analyzed all bursts detected from the 12 bursters in globular clusters, for which independent distance estimates are available. They found that for about two-thirds of the sources, the radius-expansion bursts reached $(3.79 \pm 0.15) \times 10^{38}$ erg/s. With our peak luminosity (L) calculated using the peak flux that we observed, the fraction L/L_0, where L_0 is the typical luminosity reached by PRE bursts, is approximately 0.33.

2.4 9000003888 (B3)

2.4.1 Initial Analysis

Light Curve

Burst 3 was observed in event `20200918_A09_044T01_9000003888` of neutron star 4U 1705−44 by AstroSat.
The light curve for this event is shown below:

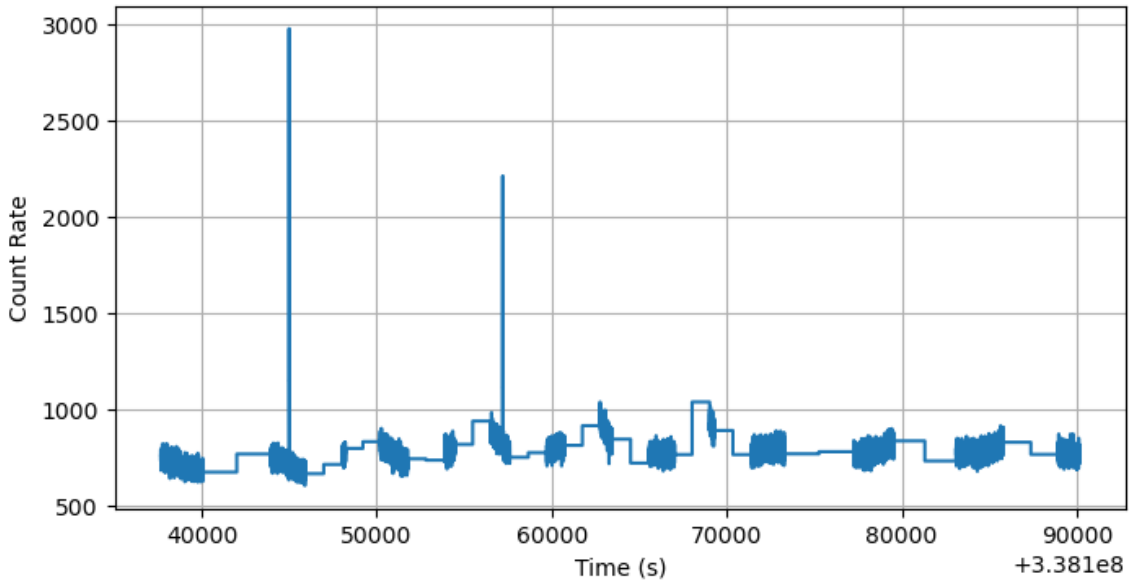

Figure 2.19: Light curve of event `20200918_A09_044T01_9000003888`, constructed from the Level-2 FITS file using the Good Time Intervals (GTIs) provided by LAXPC.

The following graph shows 2 thermonuclear (type-I) bursts. Carrying on from the previous section we will be examining the second burst of the light curve

Finding Peaks

As described perviously we use the `find_peaks` function from the `scipy.signal` module in Python. We specify a threshold peak height and a minimum distance between peaks to isolate individual burst events.
The function used is:

```
peaks, properties = find_peaks(rate, height=2000, distance=20)
```

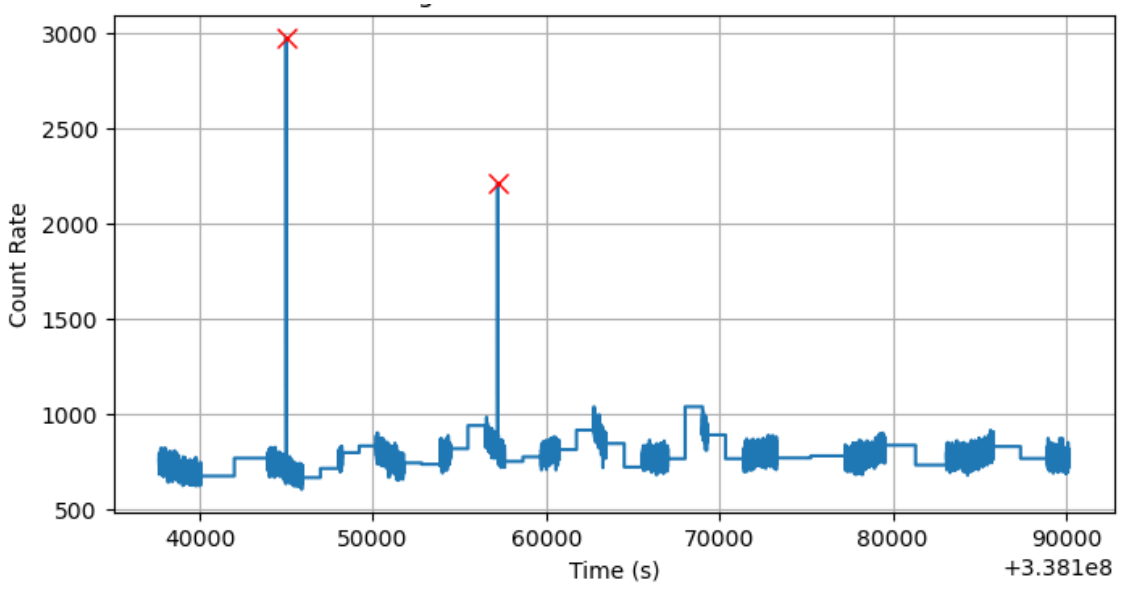

Figure 2.20: Detected peaks in the light curve of event `20200918_A09_044T01_9000003888`, constructed from the Level-2 FITS file using the Good Time Intervals (GTIs) provided by LAXPC.

Results:
The peak detection algorithm identified two candidate bursts:

- **Peak #1:** Time = 338144999.4 s, Rate = 2974.0 counts/s
- **Peak #2:** Time = 338157206.4 s, Rate = 2210.0 counts/s

In this analysis, we focus on **Peak #2**, which corresponds to the primary burst of interest.

2.4.2 Good Time Intervals (GTI)

Burst GTI Plot

To analyze the first burst in detail, we restrict the light curve to a time window centered around the burst peak. Specifically, we consider a Good Time Interval (GTI) ranging from 10 seconds before to 50 seconds after the burst peak time. This helps isolate the burst from continuous emission.

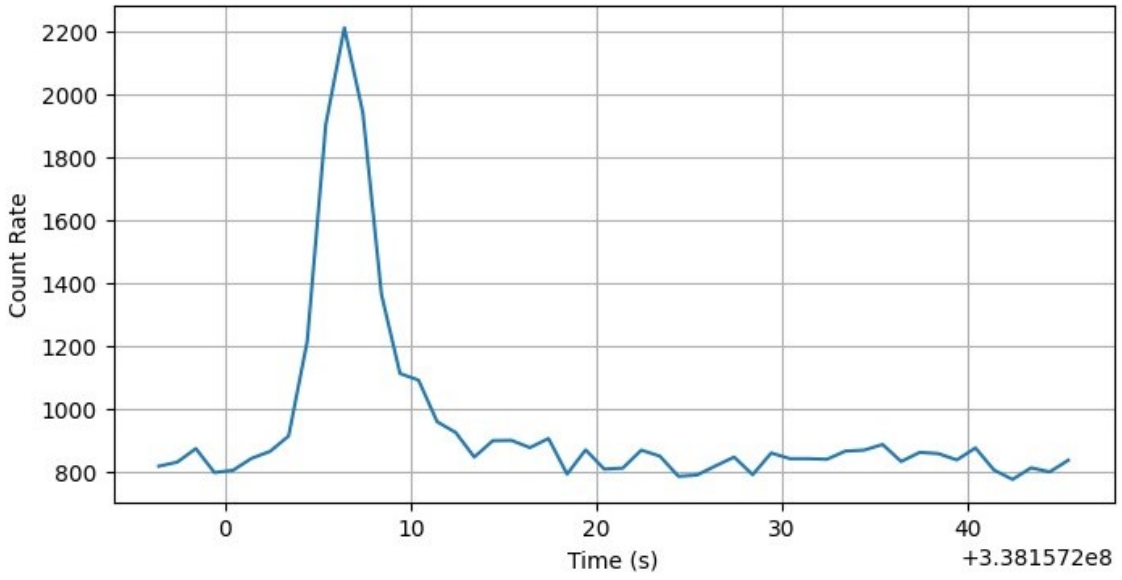

Figure 2.21: Zoomed-in light curve of B3 in event `20200918_A09_044T01_9000003888`, extracted using a GTI of $[-10\text{s}, +50\text{s}]$ around the burst peak.

We have already identified and processed emmissions from the non-burst regions in the analysis of the earlier burst

2.4.3 Fast Rise Exponential Decay Model Fit

As described previously (FRED) model is commonly used to fit gamma-ray or X-ray burst light curves.
The FRED function used in this analysis is given by:

$$I(t) = A \cdot \lambda \cdot \exp\left(-\frac{\tau_1}{t-t_s} - \frac{t-t_s}{\tau_2}\right) + C, \quad t > t_s \tag{2.2}$$

where:

- A is the pulse amplitude,
- t_s is the pulse start time,
- τ_1 is the rise timescale,
- τ_2 is the decay timescale,
- C is a offset level from origin line, and
- $\lambda = \exp\left(2\sqrt{\frac{\tau_1}{\tau_2}}\right)$ is a normalization factor.

We fit this function to the light curve using the `scipy.optimize.curve_fit` function in Python which optimize parameters to minimize the residual between the observed count rate and the model.

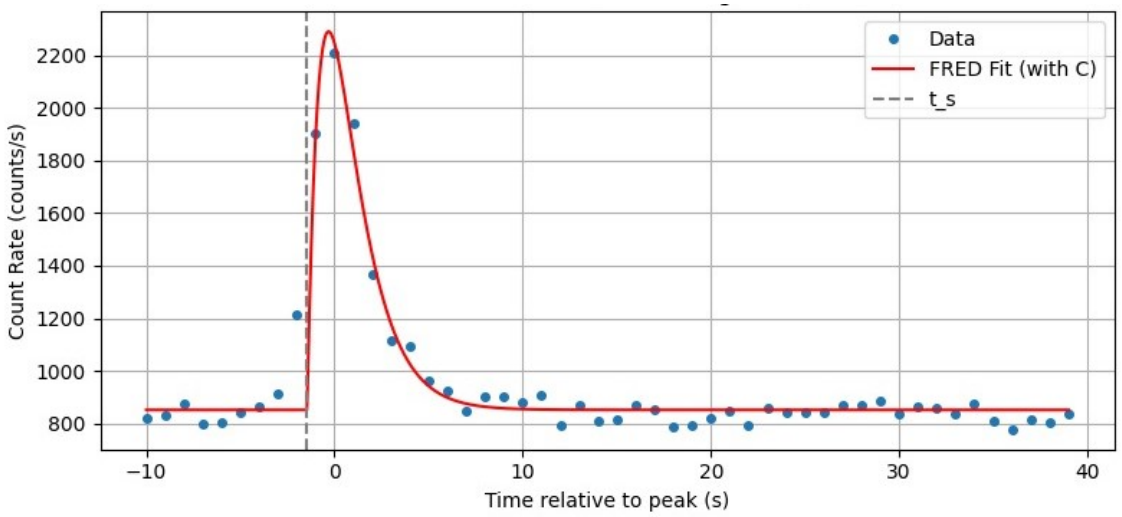

Figure 2.22: FRED model fit to the zoomed-in light curve of B3 in event `20200918_A09_044T01_9000003888`, extracted using a GTI of $[-10\,\mathrm{s}, +50\,\mathrm{s}]$ around the burst peak.

The optimized parameters obtained from the FRED model fit are listed below:

Parameter	Value
A	8865.19 ± 375.52 counts/s
t_s	338157204.96 s
τ_1	2.562 ± 0.118 s
τ_2	1.435 ± 0.012 s
C	851.463 ± 0.158 counts/s

Table 2.6: Best-fit parameters for the FRED model (with background offset C).

2.4.4 Calculation of T90

The **T90** duration is a standard measure of the temporal extent of a burst. It is defined as the time interval during which 90% of the total burst counts are detected.
Specifically:

- The **start** of the T90 interval (t_5) is the time at which 5% of the cumulative counts have been recorded.
- The **end** of the T90 interval (t_{95}) is the time at which 95% of the cumulative counts have been recorded.

$$T_{90} = t_{95} - t_5$$

The following graph shows the pulse of the FRED model with vertical lines marking t_5 and t_{95}, from which T_{90} is determined:

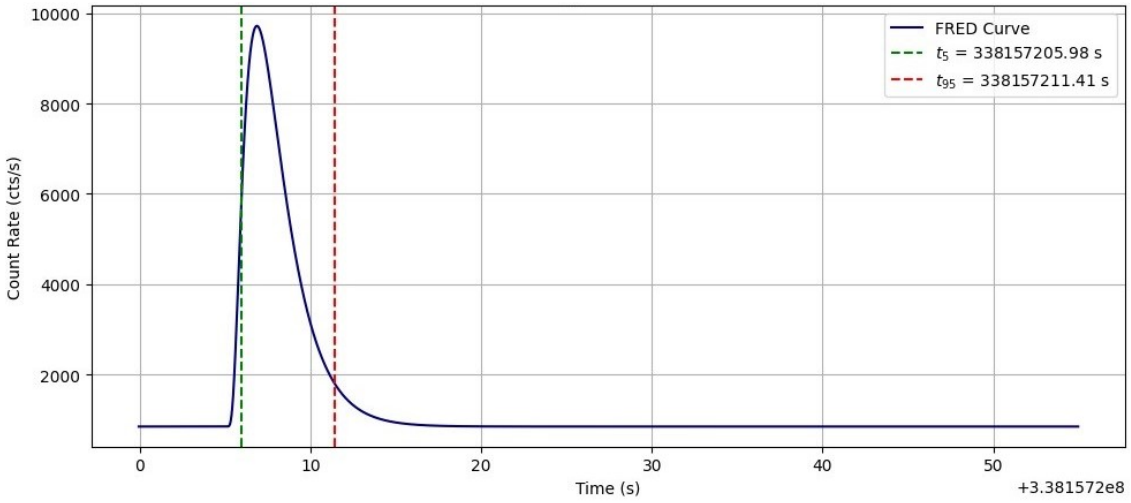

Figure 2.23: FRED model fit with vertical lines at $t_5 = 338099999.52\,\mathrm{s}$ and $t_{95} = 338100012.60\,\mathrm{s}$ used to calculate T_{90}.

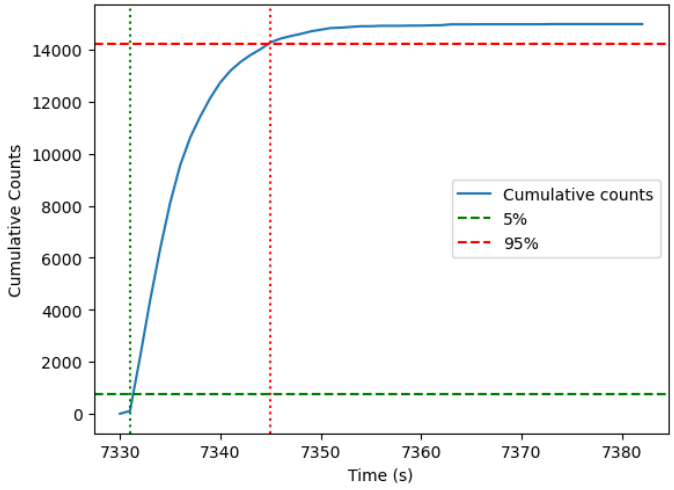

Figure 2.24: Cumulative counts for the burst region (Time is rescaled by subtracting observation start time)

Result:

$$t_5 = 338099999.52\ \mathrm{s}$$
$$t_{95} = 338100012.60\ \mathrm{s}$$
$$T_{90} = t_{95} - t_5 = 13.08\ \mathrm{s}$$

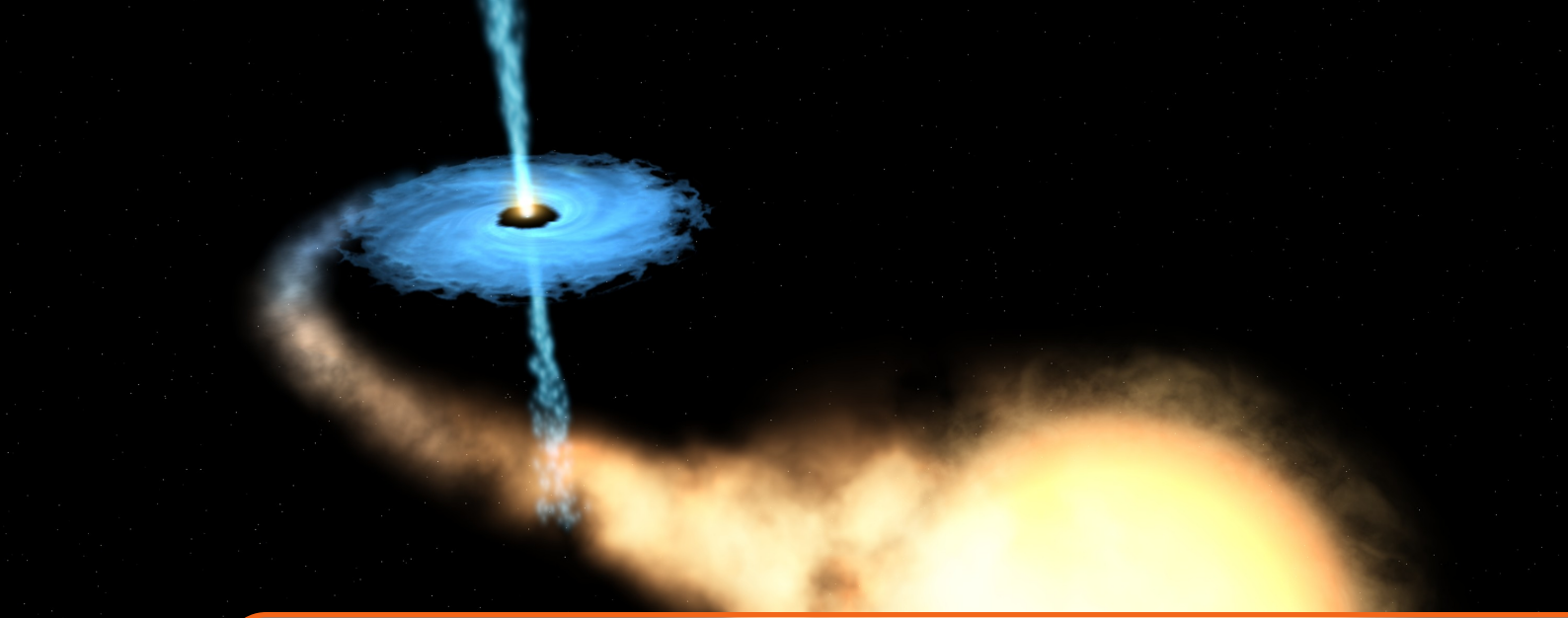

Bibliography

Articles

(Bha10) Sudip Bhattacharyya. "X-ray views of neutron star low-mass X-ray binaries". In: *arXiv preprint arXiv:1002.4480* (2010).

(GK17) Duncan K Galloway and Laurens Keek. "Thermonuclear X-ray bursts". In: *arXiv preprint arXiv:1712.06227* (2017).

(Sal23) Anirudh Salgundi. *HEASoft Installer*. `https://github.com/anirudhsalgundi/heasoft-installer`. 2023.

(Yad19) J. S. Yadav. *AstroSat/LAXPC Instrument and Performance Documentation*. `https://web.iisermohali.ac.in/web/cospar2019/pdf/jsy_iiser_mohali.pdf`. IISER Mohali, COSPAR 2019 Presentation. 2019.

(YAA+17) J. S. Yadav, P. C. Agrawal, H. M. Antia, et al. "Large Area X-ray Proportional Counter (LAXPC) on AstroSat". In: *Journal of Astrophysics and Astronomy* 38 (2017).